JACS
JOURNAL OF THE AMERICAN CHEMICAL SOCIETY

ARTICLE

pubs.acs.org/JACS

Macroporous WO_3 Thin Films Active in NH_3 Sensing: Role of the Hosted Cr Isolated Centers and Pt Nanoclusters

Massimiliano D'Arienzo,[†,*] Lidia Armelao,[‡] Claudio Maria Mari,[†] Stefano Polizzi,[§] Riccardo Ruffo,[†] Roberto Scotti,[†] and Franca Morazzoni[†]

[†]INSTM, Department of Materials Science, University of Milano-Bicocca, Via R. Cozzi 53, I-20125 Milano, Italy

[‡]ISTM−CNR and INSTM, Department of Chemical Sciences, University of Padova, Via F. Marzolo 1, I-35131 Padova, Italy

[§]Department of Molecular Sciences and Nanosystems, University Ca′ Foscari of Venezia, Via Torino 155/b, I-30172 Venezia, Italy

Supporting Information

ABSTRACT: Macroporous WO_3 films with inverted opal structure were synthesized by one-step procedure, which involves the self-assembly of the spherical templating agents and the simultaneous sol−gel condensation of the semiconductor alkoxide precursor. Transition metal doping, aimed to enhance the WO_3 electrical response, was carried out by including Cr(III) and Pt(IV) centers in the oxide matrix. It turned out that Cr remains as homogeneously dispersed Cr(III) centers inside the WO_3 host, while Pt undergoes reduction and aggregation to form nanoclusters located at the oxide surface. Upon interaction with NH_3, the electrical conductivity of transition metal doped-WO_3 increases, especially in the presence of Pt dopant, resulting in outstanding sensing properties ($S = 110 \pm 15$ at $T = 225$ °C and $[NH_3] = 74$ ppm). A mechanism was suggested to explain the excellent electrical response of Pt-doped films with respect to the Cr-doped ones. This associates the easy chemisorption of ammonia on the WO_3 nanocrystals, promoted by the inverted opal structure, with the catalytic action exerted by the surface Pt nanoclusters on the N−H bond dissociation. The overall results indicate that in Pt-doped WO_3 films the effects of the macroporosity positively combine with the electrical sensitization promoted by the metal nanoclusters, thus providing very lightweight materials which display high functionality even at relatively low temperatures. We expect that this synergistic effect can be exploited to realize other functional hierarchical metal oxide structures to be used as gas sensors or catalysts.

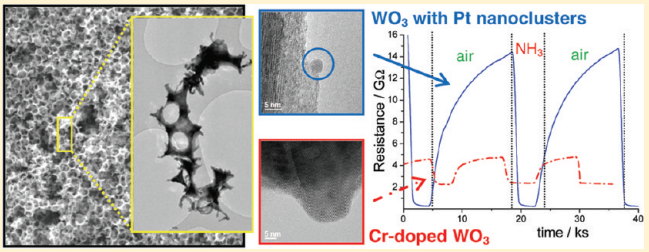

INTRODUCTION

Macroporous materials[1,2] based on metal oxides have become strategic for various applications like photonic crystals,[3−5] catalysts,[6−8] and sensor devices,[9−13] mainly due to their lightweight, their high surface area, and the well-defined porous architecture with a limited agglomerated morphology.[2] In sensing research the improvement in selectivity, reproducibility, and stability expected for the gas sensors based on macroporous metal oxides is still a challenge for pollutant detection.[14] Unfortunately, the delicate method needed to prepare macroporous materials still limits their wide employment in effective devices.[1,2]

Macroporous metal oxides are typically synthesized by alkoxide-based sol−gel processes, employing two steps:[11,15−20] (i) the self-assembling of an ordered array of colloidal microspheres of polystyrene, polymethyl methacrylate, or silica, acting as template; (ii) the filling of interstices of the structure by metal alkoxide solution, followed by sol−gel hydrolysis and densification.

The subsequent thermal treatment which removes the template leads to the macroporous structure called inverted opal, where the macropores are interconnected through holes resulting from the contact between the template spheres.[2]

The application of this synthetic method becomes particularly tricky wherein highly reactive metal alkoxides are used as oxide precursors,[21,22] or if the oxide needs to be doped by sensitizing centers,[11] for example, by transition metal atoms. Moreover, when the preparation of films is required, such as in the case of semiconductor oxide-based gas sensors, the two-step approach appears unsuitable to produce metal oxide thin films having high reproducible morphology, homogeneously embedding dopants, like transition metal centers.

To easily obtain macroporous metal oxides with high surface area and homogeneous dopant distribution, our group recently developed a novel one-step preparation of SnO_2 and Pt-doped SnO_2 as inverse opal thin films by dip-coating deposition of sol−gel precursors.[23] The procedure enables the self-assembled formation of the closely packed polystyrene (PS) microsphere array and the simultaneous infiltration of the precursors into the voids of the structure. Thus, the oxide solid skeleton around the spheres was obtained in one-step, unlike the conventional

Received: October 22, 2010
Published: March 22, 2011

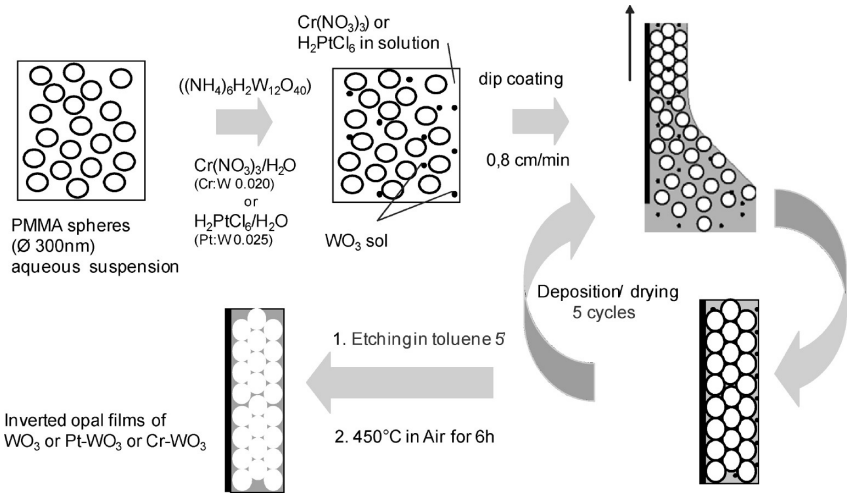

Figure 1. Schematic of one-step preparation of WO_3 inverted opal films.

sol−gel process based on the infiltration into the preformed self-assembled PS sphere array. The method is easy to be applied and fast to produce hierarchically porous layers homogeneously doped with noble metals.

The above results prompted us to apply the same one-step procedure to prepare Cr and Pt-doped WO_3 inverse opal films to be used as ammonia gas sensors. In recent years, tungsten oxide has in fact attracted great attention for its distinctive sensing properties toward NH_3 and extensive scientific and engineering research is still active on this topic, focused on optimizing sensitivity, selectivity, response rate, and long-term stability. Various strategies have been pursued including the tailoring of the oxide morphology and the doping by transition metals. In particular, many attempts have been devoted to obtain pure or transition-metal-doped nanostructured,[24−30] mesoporous[31−34] and macroporous[35−37] tungsten(VI) oxide-based materials. However either the preparation methods adopted were delicate to some extent or the sensor performances were evaluated only under relatively high ammonia concentration.

In this context, the one-step preparation of Cr and Pt-doped WO_3 inverse opal films provides an easy way to produce macroporous structures very suitable for ammonia detection. Furthermore, successful and controllable doping sensitization is performed by simply adding the metal precursor to the starting aqueous solution, guaranteeing an easy and homogeneous dispersion of the dopant.

The morphology of the films and the electronic properties of both WO_3 and the doping centers were also investigated in order to suggest a mechanism for the variations of electrical sensitivity in the presence of NH_3. The effect of the macroporous structure on the electrical response was also discussed in terms of conductance regime under different gas concentrations, in order to achieve optimum balance between the intensity and the reproducibility of sensor performances.

EXPERIMENTAL SECTION

Chemicals. Methyl methacrylate (MMA, 99%), 2,20-azobis (2-methylpropionamidine) dihydrochloride (97%), ammonium metatungstate ($(NH_4)_6H_2W_{12}O_{40}$, 99.9%), chromium(III) nitrate nonahydrate ($Cr(NO_3)_3 \cdot 9H_2O$, 99%) and chloroplatinic acid hydrate ($H_2PtCl_6 \cdot xH_2O$, 99.995%) were all purchased from Aldrich and used without further purification.

Synthesis of Polymethylmethacrylate Spheres. An aqueous suspension of monodispersed poly(methyl methacrylate) (PMMA) microspheres (∅ = 450 ± 5 nm) was synthesized according to the Schroden standard technique.[38] The size of the PMMA spheres produced using this method is highly dependent on the composition of the synthesis mixture and the reaction temperature. Briefly, MilliQ water (400 mL) and methyl methacrylate (MMA, 100 mL) were charged into a 4-necked round-bottomed flask (500 mL in volume), equipped with a mechanical stirrer (glass shaft with Teflon stirrer blade), water-cooled reflux condenser, nitrogen bubbler, and a glass quick-fit stopper. The mixture was then heated to 70 °C, whereupon 2,20-azobis(2-methylpropionamidine) dihydrochloride (0.375 g) was added as an azo-initiator and the polymerization of the MMA started. The reaction mixture was maintained at 70 °C for 2 h under vigorous mechanical stirring and then cooled to room temperature over 3−4 h under a nitrogen purge. The resulting colloidal suspensions of PMMA spheres was finally filtered through a glass wool plug to remove large agglomerates and stored in PET bottles for later use.

Preparation of Precursors Suspensions of Undoped and Cr/Pt-Doped WO_3 Inverted Opals and Film Deposition. WO_3 precursor suspension was prepared by dissolving 0.3460 g of $(NH_4)_6H_2W_{12}O_{40}$ in 5 mL of the colloidal aqueous suspension of PMMA microspheres. The mixture obtained was stirred at room temperature for several minutes until a homogeneous suspension was obtained. (Cr/Pt)-doped WO_3 precursor suspension (Cr:W molar ratio 0.020 or Pt:W molar ratio 0.025) was prepared by simply adding the proper amount of $Cr(NO_3)_3 \cdot 9H_2O$ or $H_2PtCl_6 \cdot x\ H_2O$ to the WO_3 suspension. The inverted opal films were prepared by the one-pot procedure[23] using the dip-coating method. Suprasil quartz slides (20 × 20 mm, 0.25 mm thickness) were used as the substrates.

In a typical deposition, the substrate was settled vertically into the WO_3/PMMA or the Cr/Pt-doped WO_3/PMMA sol phase for several minutes and then withdrawn at the constant rate of 0.8 cm/min. The procedure allows the self-assembly of the close-packed PMMA array, acting as the template, and the simultaneous infiltration of the suspension precursor into the PMMA structure, thus obtaining a solid skeleton around the spheres. After the deposition, the film was dried in air for about 10 min at 60 °C. The above cycle was repeated five times; then the films underwent etching treatment with toluene for 5 min in order to remove the most of the organic template. Finally, they were annealed at 450 °C (heating rate 2 °C min^{-1}) in air stream (80 cm^3 min^{-1}) for 5 h to fully decompose the

dx.doi.org/10.1021/ja109511a |J. Am. Chem. Soc. 2011, 133, 5296–5304

PMMA remnants. The scheme of the one-step deposition of the macroporous WO_3 films is reported in Figure 1.

Morphological and Chemical Characterization. Scanning electron microscopy (SEM) measurements on the inverse opal films were performed by a Vega TS5136 XM Tescan microscope in a high-vacuum configuration. The electron beam excitation was 30 kV at a beam current of 25 pA, and the working distance was 12 mm. In this configuration the beam spot was 38 nm. Prior to SEM analysis, samples were gold-sputtered. Elemental mapping on WO_3 layers was performed by an EDAX Genesis 4000 XMS Imaging 60 apparatus.

High-resolution transmission electron microscopy (HRTEM) and electron diffraction (ED) were performed using a Jeol 3010 apparatus operated at 300 kV with a high-resolution pole piece (0.17 nm point-to-point resolution) and equipped with a Gatan slow-scan 794 CCD camera. Samples were obtained by removing a film portion from the substrates in order to obtain a fine powder sample, then suspended in 2-propanol. A 5 μL drop of this suspension was deposited on a holey carbon film supported on a 3 mm copper grid for TEM investigation.

The surface chemical composition of the films was investigated by X-ray photoelectron spectroscopy. Analysis was performed on undoped, Pt- and Cr-doped WO_3 layers annealed in an air stream (50 cm^3 min^{-1}) or NH_3 (74 ppm)/air stream (50 cm^3 min^{-1}) at 300 °C. Samples were transferred into the fast entry lock system of the XPS vacuum chamber without ambient exposure in order to avoid surface modification or atmospheric contamination. The analysis was performed with a Perkin-Elmer Φ 5600-ci spectrometer using nonmonochromatized Al−Kα radiation (1486.6 eV). The sample analysis area was 800 μm in diameter and the working pressure lower than 10^{-9} mbar. The spectrometer was calibrated by assuming the binding energy (BE) of the Au $4f_{7/2}$ line at 83.9 eV with respect to the Fermi level. The standard deviation for the BEs values was ±0.2 eV. Survey scans were obtained in the 0−1300 eV range. Detailed scans were recorded for the C1s, O1s, Cr2p, Pt4f, and W4f regions. No further element was detected. The samples were sufficiently electrically conductive at room temperature so that no compensation for charging effects was required. The residual BE shifts (on the order of <0.5 eV) were corrected by assigning to the C1s peak associated with adventitious hydrocarbons a value of 284.8 eV.[39] The analysis involved Shirley-type background subtraction, nonlinear least-squares curve fitting, adopting Gaussian−Lorentzian peak shapes, and peak area determination by integration. The atomic compositions were evaluated from peak areas using sensitivity factors supplied by Perkin-Elmer, taking into account the geometric configuration of the apparatus. The experimental uncertainty on the reported atomic composition values does not exceed ±5%.

Electrical Measurements. Suprasil quartz slides were equipped, before film deposition, with two gold current collectors (20 mm) deposited at a distance of about 2 mm from each other by the dc sputtering technique. Then the samples were placed in a quartz chamber sited in an oven, and the measurements were performed at different temperatures, ranging from 200 to 300 °C. The electrical resistance was measured by a programmable electrometer controlled by a PC. To dynamically reproduce environmental conditions in a controlled and repeatable way, a system based on volumetric gas mixing through mass flow controllers and certified bottles was used. The sensing element was initially equilibrated in air flow (100 mL min^{-1}) at the selected temperature, and then NH_3 (6.2−74 ppm)/air mixture was introduced (100 mL min^{-1}) up to equilibrium conditions. The different gas mixtures were obtained by dilution of the starting NH_3 (74 ppm)/air mixture using mass flow controllers. The initial resistance conditions of the film were restored by air equilibration, before again introducing the NH_3/air mixture. S is the electrical response defined as the ratio between the film resistance under flowing air, R_{AIR}, and under flowing NH_3/air mixture, R_{MIX}, respectively ($S = R_{AIR}/R_{MIX}$).

The reliability as well as the reproducibility of the devices is certainly satisfactory; in fact, all the produced sensors (at least two for each material) were working, and the response reproducibility (obtained by at least six pulses) was calculated to be ±14%.

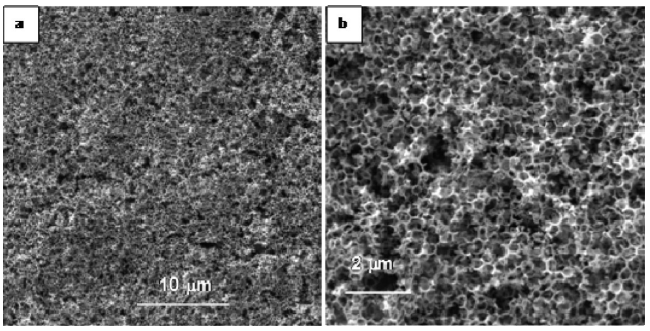

Figure 2. SEM micrographs of Cr-doped WO_3 inverted opal films showing reasonably uniform layers with no evident cracks.

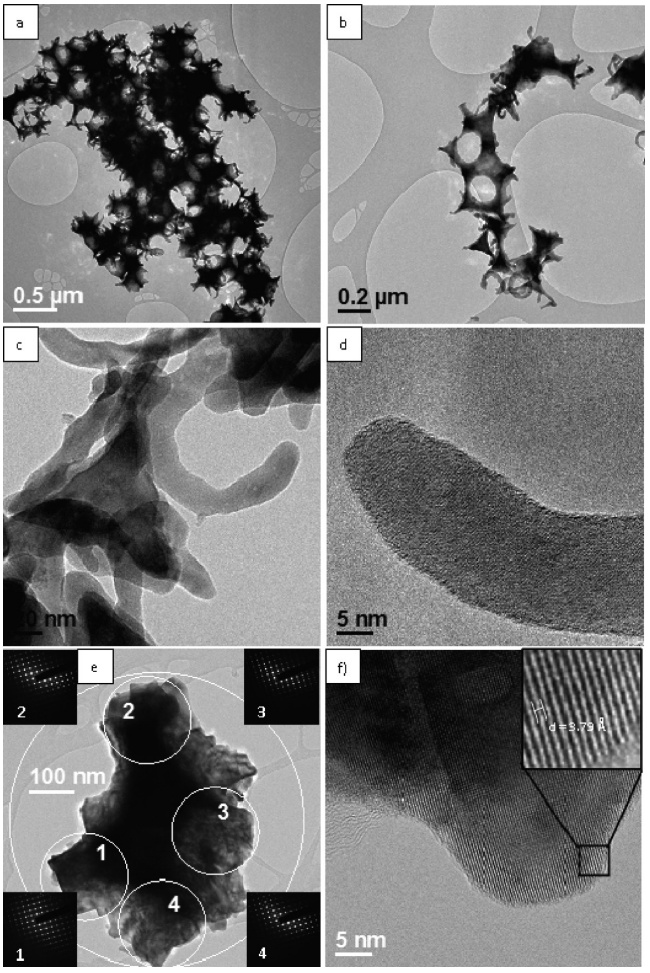

Figure 3. TEM (a, b, c, e) and HRTEM (d, f) images of Cr-doped WO_3 inverted opal films. Insets in panel e report the ED patterns collected in the selected 1−4 zones of the WO_3 large single crystallite in the white ring. Inset in panel f reports the crystal structure of WO_3 lattice.

RESULTS AND DISCUSSION

Morphological Investigation. Scanning electron microscopy (SEM) investigations performed on both undoped and transition metal-doped WO_3 films revealed the presence of the inverted

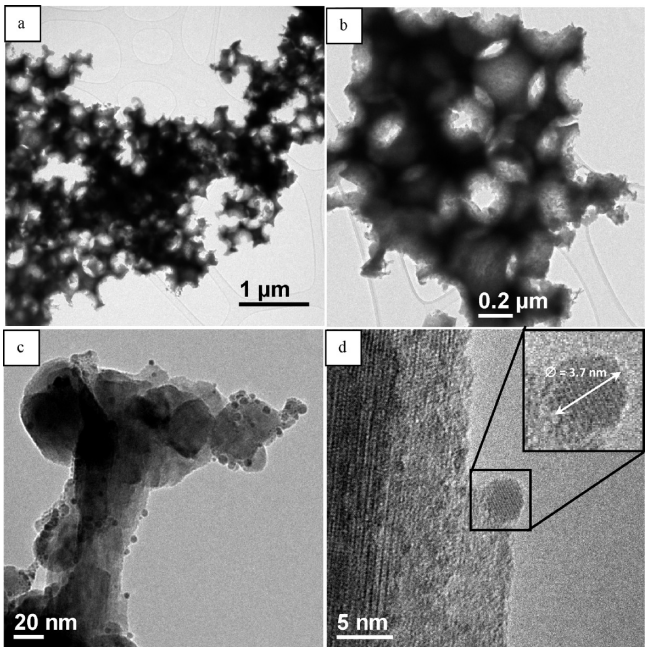

Figure 4. TEM (a, b, c) and HRTEM (d) images of Pt-doped WO_3 inverted opal films. Insets in panel d report a magnification with the average diameter of the Pt cluster anchored to the WO_3 surface.

opal structure. As examples, Figure 2 reports SEM images of macroporous Cr-doped WO_3 films. No pore occlusions were detectable and films with extensive homogeneity were obtained. X-EDS (energy dispersive X-ray analysis) investigation performed in conjunction with SEM analysis revealed the uniform distribution of the Cr(III) centers across the oxide layer (see Figure S1, Supporting Information). Similar images were acquired for undoped WO_3 films, confirming that doping by transition metal ions does not affect the macroporous structure (Figure S2, Supporting Information).

These results clearly indicate that, besides decreasing the number of synthetic steps in the fabrication of inverse opal films, the one-step deposition guarantees the formation of closely packed PMMA arrays and the simultaneous permeation of the WO_3 precursor solution into the opal structure voids, also preventing cracks upon drying both at the colloidal assembly and the infiltration stages.

The macropore size, measured from the distance between the centers of two neighboring hollow spheres, resulted in 300 ± 5 nm, a value lower than that of the parent PMMA size (450 ± 5 nm) due to both shrinkage of PMMA above the glass transition temperature (ca. 105 °C) and sintering of WO_3.

TEM and HRTEM images of Cr-doped WO_3 inverted opal films are shown in Figure 3. No amorphous surface layers were detectable. WO_3-based inverse opal consists of irregular shaped highly interconnected nanoparticles surrounding the hollow spheres (Figure 3a,b). It is interesting to note that the WO_3 structure is built up of large nanocrystals grown around the template spheres (Figure 3c,d, average length > 50 nm), unlike the small cassiterite nanoparticles (average sizes: ca. 5−6 nm) surrounding the hollow spheres of the tin oxide inverse opals described in our previous study.[23]

In micrometric zones of the inverse opal structure (Figure 3e), very large single crystallites of WO_3 (indicated by the white ring) grown around the macropores were detected. The ED patterns

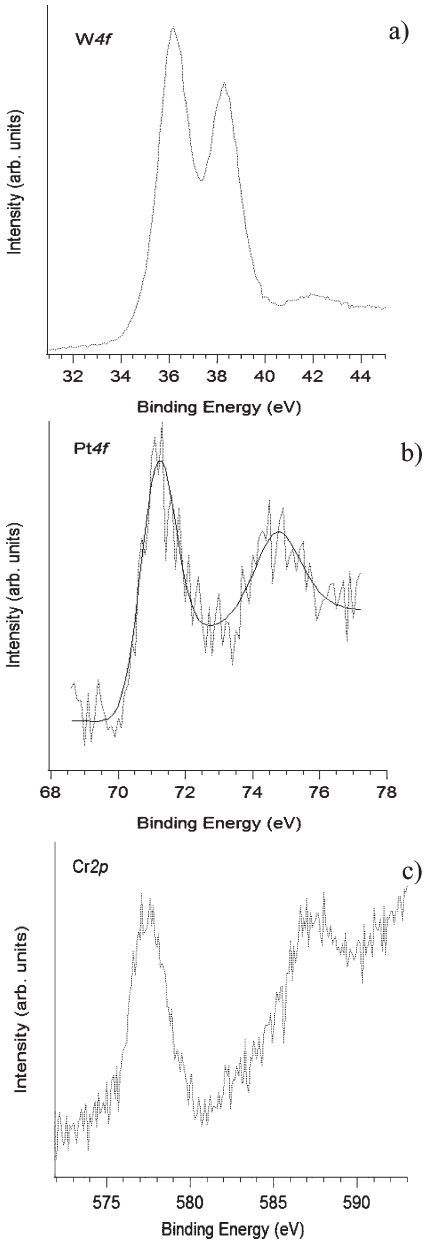

Figure 5. (a) XPS W4f spectrum of the pure WO_3 films after annealing in air. (b) XPS Pt4f spectrum of the Pt-doped WO_3 films after annealing in air. The experimental data were fitted to a single component that is also shown (continuous line). (c) XPS Cr2p spectrum of the Cr-doped WO_3 films after annealing in air.

collected in zones 1−4 are identical and continuous fringes are detected, thus demonstrating the single crystal nature. A representative high-resolution HRTEM image of a portion of a WO_3 nanocrystal is shown in Figure 3f. The figure inset shows that the lattice fringes of the nanocrystal have a spacing of 3.79 Å, which reasonably matches the interplanar distance of the (020) plane of the monoclinic tungsten trioxide (ICDD 71-0131). TEM analysis performed on undoped WO_3 inverted opal films gave analogous results (Figure S3, Supporting Information).

Finally, the HRTEM images (Figure 3d,f) prove that Cr-doped inverse opal films are exempt of metal clusters or secondary phases, in agreement with an homogeneous dispersion of the dopant in the oxide matrix.

Figure 4 reports the TEM and HRTEM images of the macroporous Pt-doped WO_3. The skeletal structure resembles that observed for Cr-doped inverse opal films (Figure 4a) with large nanocrystals surrounding the voids generated by the PMMA spheres (Figure 4b). Higher magnification (Figure 4c) reveals instead the presence of numerous Pt metal clusters anchored on the WO_3 surface. Owing to the high density of noble metals, these Pt nanoparticles possess darker contrasts under TEM observation.

In particular, Figure 4d shows a single spherical Pt nanoparticle, anchored to the WO_3 surface, with a measured diameter of ca. 3.7 nm and calculated interplanar spacing of 2.25 Å (not shown); this distance is in agreement with the (111) crystallographic plane of Pt (JCPDS 04-0802). Pt clusters are homogeneously distributed throughout the film (Figure 4c) and seem to be mainly located at the surface of crystallites. The segregation of platinum in nanoclusters suggests a strong tendency of WO_3 lattice, in the form of inverted opal, to remain undistorted as large single crystals, as clearly revealed by HRTEM images previously described. Pt centers, which are reduced within the WO_3 lattice more easily than Cr centers, can move and aggregate into clusters through the channels of the open perovskite structure.

XPS Investigation. XPS analysis was performed on undoped, Pt- and Cr-doped WO_3 sol−gel films[40] treated in air stream (50 cm^3 min^{-1}) or NH_3 (74 ppm)/air stream (50 cm^3 min^{-1}) at 300 °C. A common observed feature for the films is the position of the main spin−orbit split component ($j = {}^7/_2$) of the W4f peak at 36.1 eV, which is typical for W(VI) sites coordinated by oxygen atoms (Figure 5a).[41] No variations in the W4f profile or energy position were recorded depending on the doping with different species or under different annealing atmosphere. In addition, the nature of the O1s peak (BE = 530.5 eV) supports the formation[37] and chemical stability of the WO_3 network for all the samples.

Doping of WO_3 layers with platinum led to the formation of zerovalent species of the noble metal, as it was observed from the analysis of Pt-related XPS lines. This was probably caused by the initial presence of the PMMA template that produces a reducing environment around the platinum centers during the final thermal annealing. Pt4f band shape (Figure 5b) and peak position (BE $Pt4f_{7/2} \approx 71.2$ eV, $j-j$ doublet separation ≈ 3 eV)[41] indicated that platinum was dispersed in the tungsten oxide layers in the form of Pt(0) centers only, and no variation in the platinum chemical state was observed depending on annealing conditions. The surface Pt/W atomic ratio was ∼0.006 in the WO_3 layers, which corresponds to about one-fourth of the nominal value. This apparent depletion could be tentatively explained considering that a fraction of the Pt nanoparticles dispersed on the surface are larger than the sampling depth of XPS.

In the Cr-doped WO_3 films, chromium retained the chemical state of the precursor compound; this was ascribed to the low reducibility of Cr centers by the PMMA matrix. Indeed, the $j = {}^3/_2$ component of the Cr2p line was peaked at 577.4 eV ($j-j$ doublet separation ≈ 10 eV), that is typical for Cr(III) centers dispersed in an oxide environment[41] (Figure 5c). As in the previous case, the chemical state and/or environment of the doping species did not appear affected by the different annealing conditions. At variance with Pt-doped WO_3 films, the surface Cr/W atomic ratio was ∼0.035, that is, significantly higher that the nominal value. This effect is probably related to the high mobility of Cr ions, which can easily diffuse through the WO_3 structure thus reaching the oxide surface.

Electrical Measurements. As already mentioned, WO_3 is considered one of the most promising materials for ammonia gas detection.[24−26,29,30,34] The electrical response to this gas was associated with specific reactions and species active at the solid−gas interface[9a]. In particular, we suggested that ammonia molecules chemisorb on both Lewis and Brønsted acidic sites at the WO_3 surface (reactions 4, 5).[24,25] If not simply desorbed, NH_3 can undergo dehydrogenation, mainly through the capture of hydrogen atoms by the oxygen lattice centers (O_O), forming hydroxyl groups. This process generates NH_{3-n}^{n-} species ($n = 1$, 2, 3) which can interact with other NH_{3-n}^{n-} species leading to the formation of molecular nitrogen by reaction 6A. Otherwise, they can react with an oxygen center to form nitrogen monoxide, reaction 6B, being this the favored path in an oxygen-containing atmosphere. Finally, NH_{3-n}^{n-} species may reduce NO to N_2O by reaction 6C. The whole process is described as follows:[24]

$$NH_3 \rightleftarrows M-NH_3 \quad (M = W, Cr, Cu, V) \tag{4}$$

$$NH_3 + M-OH \rightleftarrows M-O^-NH_4^+ \quad (M = W) \tag{5}$$

$$2NH_3 + 6O_O \rightleftarrows 2NH_{3-n}^{n-} + \underset{\text{reaction (6B)}}{\overset{\text{reaction (6A)}}{2n\,O_OH}} + (6-2n)O_O \xrightarrow{+2NO} \text{reaction (6C)}$$

$$\rightleftarrows N_2 + 6O_OH + 6e^- \rightleftarrows N_2 + 3H_2O + 3O_O + 6e^- \tag{6A}$$

$$\rightleftarrows 2NO + 6O_OH + 10e^- \rightleftarrows 2NO + 3H_2O + 3O_O + 10e^- \tag{6B}$$

$$\rightleftarrows 2N_2O + 6O_OH + 6e^- \rightleftarrows 2N_2O + 3H_2O + 3O_O + 6e^- \tag{6C}$$

All these electron donor processes increase the WO_3 conductance improving its electrical sensitivity.

We also suggested that, in the presence of doping metal centers, the doping transition metal decreases its positive oxidation state by trapping the electrons given through reactions (6A−6C):[21,23]

$$M^{m+} + ne^- \rightarrow M^{(m-n)+} \quad (m, n = 1, 2, 3, 4) \tag{7}$$

As a consequence, reactions 6A−6C undergo right-hand shift and produce further electrons, increasing the electrical response of the material.

On the basis of the above properties, WO_3 inverse opal films are expected to combine the electronic sensitizing effects of the doped metal centers with the advantages of the macroporous morphology well suited to fast gas diffusion, thus obtaining better sensor performances.

WO_3-based inverse opal films showed decreased resistance under NH_3, while increase under air, thus confirming the n-type semiconductor behavior. Moreover the response of the sensing layers increases on increasing the ammonia concentration (Figure 6).

The sensor response was evaluated as $S = R_{AIR}/R_{MIX}$, where R_{AIR} is the resistance under air and R_{MIX} is the electrical resistance under NH_3/air mixed gas. The variations of the electrical response were taken at different temperatures (200−300 °C) and for different NH_3 concentrations (6.2−74 ppm) in dry air.

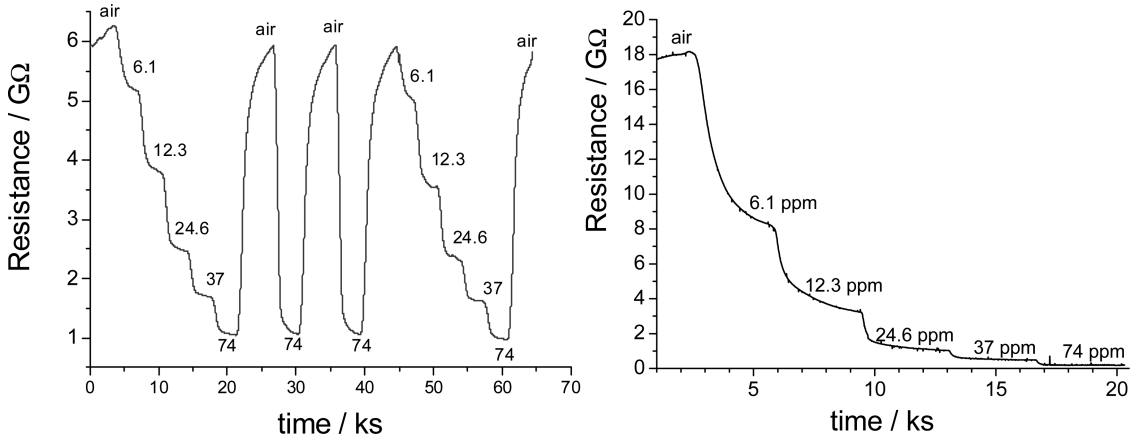

Figure 6. Examples of electrical responses of (left) Cr-doped and (right) of Pt-doped WO_3 inverse opal films to different concentrations of NH_3 in synthetic air. The responses are measured at 300 and 250 °C, respectively.

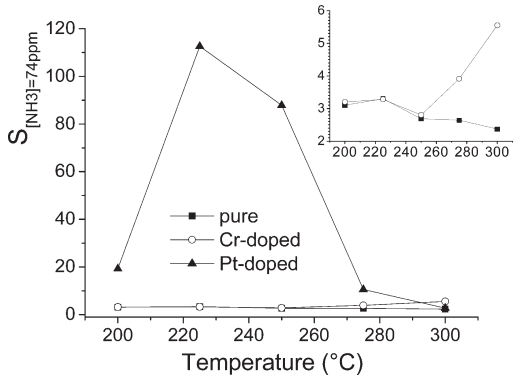

Figure 7. Comparison among the electrical responses of pure and doped inverse opal films at different temperatures recorded for 74 ppm [NH_3] in dry air. The inset highlights the difference between undoped and Cr-doped sensor responses.

Figure 7 reports the electrical responses as a function of the operating temperatures of undoped, Cr-doped, and Pt-doped WO_3 inverse opal films under NH_3 (74 ppm)/air, which is the highest used NH_3 concentration. The Pt-doped layer shows outstanding performances between 200 and 250 °C with a remarkable maximum *S* value of 110 at 225 °C. The undoped sensor has similar temperature dependence although the response is much lower (*S* maximum = 3.3 at 225 °C, see inset in Figure 7). The Cr-doped WO_3 films display their highest *S* value at 300 °C, in accordance to the results recently reported by Morante et al.[34] This suggests that the interaction of NH_3 with Cr-doped WO_3 is fully under kinetic control. The maximum shaped trend of electrical sensitivity, particularly evident in Pt-doped layers, is probably caused by the presence of NO, a side product of the ammonia oxidation (reaction 6B). In fact, NO easily transforms into NO_2 which acts as oxidizing agent and increases the layer resistance. Upon heating, the sensor response increases by interaction with ammonia while it decreases by interaction with NO_2. The overall balance between the two opposite effects generates the maximum in the electrical response trend. At high temperature the NO_2 oxidizing effect is prevalent, while at low temperature, being the conversion of NH_3 to NO less favored, the NH_3 reducing effect prevails.

To better detail the electrical sensitivity toward ammonia, we report the electrical response of all layers as a function of NH_3 concentration at several temperatures (Figure 8). At each temperature, layers generally discriminate well the different concentration of ammonia (see also Figure 6).

The electrical response of Cr-doped WO_3 is generally comparable with pure WO_3 (insets of Figure 8a and 8b) at low temperatures, instead it becomes considerably higher above 275 °C (Figure 8d). This also confirms that the doping with chromium improves the electrical response of WO_3 films. In principle Cr^{3+} centers should accept the electrons injected by NH_3 (following reaction 7), and it is therefore expected that Cr^{3+} centers, interacting with ammonia, decrease their positive oxidation state. Nevertheless, no direct evidence of their reduction was obtained (see XPS data), probably because the amount of reduced centers is below the XPS detection limits. The Pt-doped WO_3 layers showed once again the best performances at temperature below 300 °C; in fact, even a very low NH_3 concentration (6.2 ppm) induces appreciable changes of electrical resistance in Pt-doped WO_3 inverse opal films, being $S = 2.9$ and 2.0 at 225 and 250 °C, respectively.

The reason for the higher electrical sensitivity of Pt-doped WO_3 layers cannot be attributed to higher amounts of electrons trapped by Pt centers, because no oxidized Pt^{m+} centers were detected before interaction with NH_3. Instead, it may be suggested that the Pt nanoclusters anchored to the WO_3 surface, well evident from both HRTEM and XPS investigations, act as catalysts of the interaction between ammonia and O_o centers decreasing the activation barrier in the reactions (6). Similar behavior was recently reported in the literature and was attributed to the easy dissociation of the N−H bond, in the presence of Pt or noble metals centers.[46]

The electrical measurements performed on pure and doped sensors also revealed that the high sensitive Pt-doped WO_3 films have recovery time which is three times higher than Cr-doped and undoped films. The reason for this behavior is difficult to explain; we can tentatively propose that the capture of electrons by oxygen, expected during air pulse, produces negatively charged oxygen forms. These forms should be more easily chemisorbed at the surface in the presence of positively charged transition metal ions (Cr^{n+}) than of zerovalent Pt metal clusters. Thus Pt-doped films, re-exposed to air, need longer times to readsorb the oxygen species and return to the initial

dx.doi.org/10.1021/ja109511a |*J. Am. Chem. Soc.* 2011, 133, 5296–5304

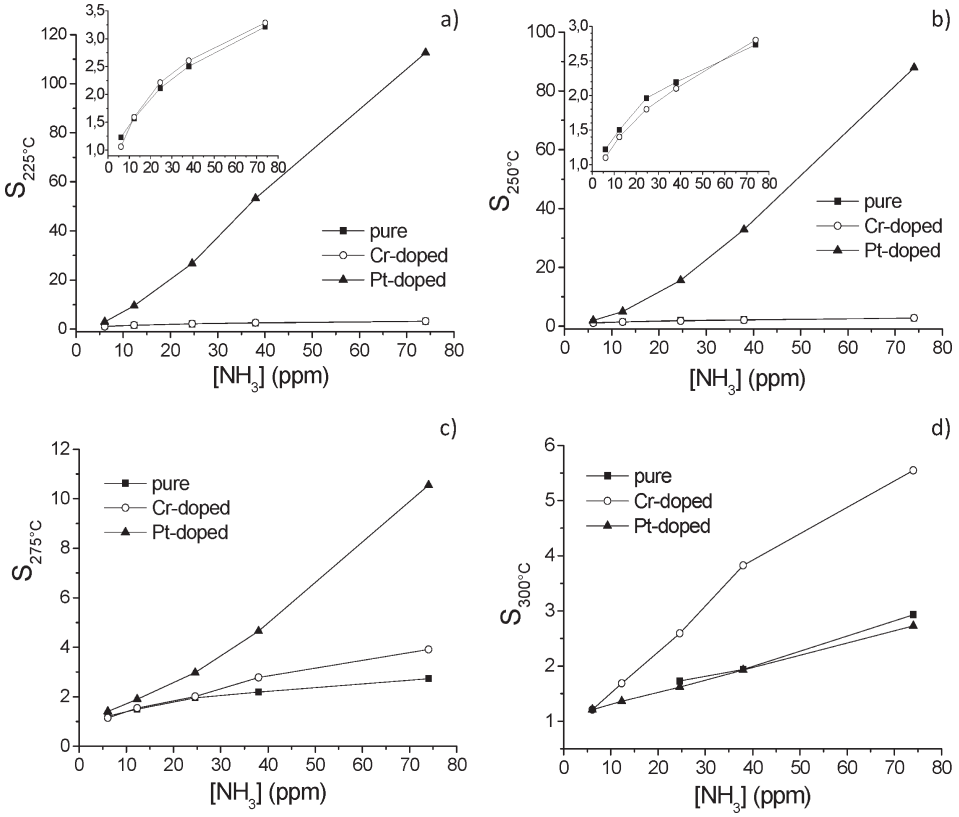

Figure 8. Comparison among the electrical responses of pure and doped inverse opal films as a function of ammonia concentration in dry air at different temperatures: (a) 225, (b) 250, (c) 275, (d) 300 °C. Insets in panels a and b highlight differences between undoped and Cr-doped sensor responses which are difficult to appreciate in the full scale.

resistance. The electrical responses as well as the recovery times (i.e., the time to re-equilibrate the sensing element in dry air after exposure to the NH_3 highest (74 ppm) concentration) of the sensors are reported in Table S1 (Supporting Information).

To discriminate the effect of the hierarchical structure on the sensing properties from those of the sensitizing metal centers, we examined the behavior of nanostructured Pt-doped WO_3 films obtained by a sol−gel conventional method(s).[33] These layers display, similarly to the corresponding opal films, small Pt nanoclusters, apparently within the layer (see Supporting Information). In this case, under the same conditions that evidenced the outstanding electrical sensitivity of inverse opal layers (T = 225 °C and [NH_3] = 74 ppm), the response of the conventional sol−gel material ($S = 30 \pm 4$) was still high but remarkably lower than the value found for the of inverted opal sol−gel films ($S = 110 \pm 15$). This confirms that the very high accessibility of the macroporous structure promotes the diffusion and transport of ammonia into the sensing layer, and this effect, together with the electronic sensitization promoted by the Pt nanoparticles located at the surface, further enhances the electrical sensitivity of the opal films.

Accurate comparison among the electrical responses of the macroporous WO_3 films and those of other systems reported in literature is difficult to achieve due to differences in the sensing layer composition, as loading and kind of metal dopant, and in the operating conditions, as gas concentration and temperature. However, the sensitivity of macroporous Pt-doped films synthesized in this work, at low operating temperature (225 °C) and in the examined NH_3 concentration range (6.2−74 ppm), resulted much higher than those reported for conventional WO_3 films doped with Pt[29,30] or other metals.[24,34,42,47−49]

Figure 9 reports in a double logarithmic plot the variation of the electrical resistance of the doped WO_3 inverted opal films versus NH_3 concentration. The linear trend can be related to the conductance model limited by the electron transport across the intergranular Shottky barrier[50−52] where

$$\sigma \propto \exp[-\mathrm{eV_s}/kT] \qquad (8)$$

(σ is the conductance and eV_s represents the surface barrier height at the intergranular contact).

According to this model, the response of the WO_3 inverse opal films is explained by using the following equation:[9,10,52]

$$\sigma/\sigma_0 = A_g p_g^{\beta} \quad \text{or} \quad \log \sigma/\sigma_0 = A_g + \beta \log p_g \qquad (9)$$

where σ_0 denotes the conductance in the absence of the target gas, p_g is the gas partial pressure, A_g is a prefactor, and β is the response order. Mechanisms were formulated to describe the surface reaction and predict the β value in eq 9.[9,10] This is usually 1 or 1/2, depending on the charge state of the surface species, the stoichiometry of the elementary surface reactions, and the microstructure of the material.[9,10] These properties contribute by different weight to the fluctuations of the response order value.

To reproduce the β parameter in eq 9, models were constructed which account for structural properties.[53,54] Ozin et al.,[9] developed a simplified model, in which the SnO_2 inverted opals were represented as sphere "agglomerates". In particular, they

dx.doi.org/10.1021/ja109511a |J. Am. Chem. Soc. 2011, 133, 5296–5304

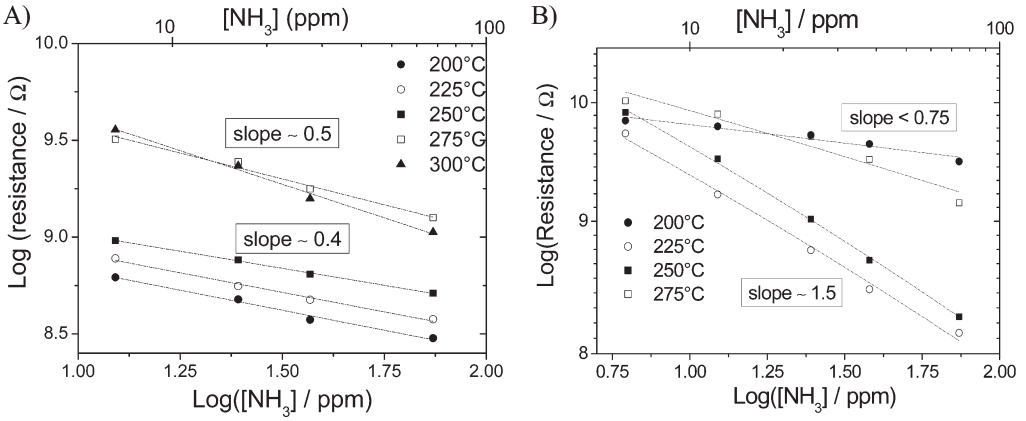

Figure 9. Resistance variation for Cr-doped (A) and Pt-doped (B) WO_3 inverted opal films after exposure to pulses of NH_3/air (6.2−74 ppm) at different operating temperatures (200−300 °C).

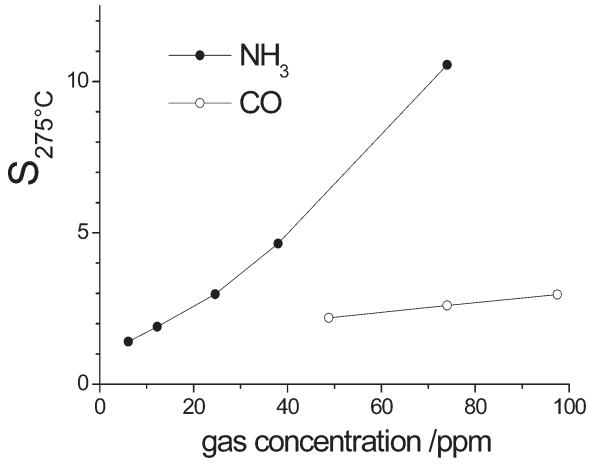

Figure 10. The electrical responses of Pt doped inverse opal films as a function of ammonia and carbon monoxide concentrations in dry air at 275 °C.

assigned a response exponent value of 0.5 to a fully regular nanoparticles microstructure. They also stated that the presence of disordered microstructures or local agglomeration is expected to shift β from this ideal value.

In the case of Cr-doped WO_3 films (Figure 9A), the calculated β value (i.e., the slope of the curve described by eq 9) was similar or slightly lower than 0.5 at each temperature. This is in agreement with the relatively regular array of WO_3 nanocrystals found in the inverse opal structure (see TEM micrographs, Figure 4a,b) and can be associated with a surface reactivity similar to that described for SnO_2 materials.[23] Differently, Pt-doped WO_3 sensors show β values as always higher than 0.5 (Figure 9B); this can be reasonably ascribed to the presence of Pt nanoclusters which may induce disordered zones in the inverse opal structure and give rise to a different sensing mechanism at the microscale level.

Finally, the β values calculated for Pt-doped WO_3 films are temperature dependent. Since the inverse opal structure of Pt-doped WO_3 layers does not change upon heating, the variation of β can be related to a variation in the dehydrogenation mechanism of NH_3 at the WO_3 surface, probably associated to a temperature dependent N−H bond dissociation.[46]

To evaluate the NH_3 selectivity of the Pt-doped WO_3 sensing element, we have measured the electrical responses in CO/air gas mixtures having a similar concentration range (Figure 10). In particular, the material presents S value of 2.6 at 74 ppm of CO which is about 4 times less that in NH_3. Although the system senses also other reductive gas, it shows a good selectivity toward ammonia which is an intrinsic property of WO_3, as already reported in literature.[29]

CONCLUDING REMARKS

One-step deposition of undoped and Cr or Pt-doped WO_3 inverted opal films, to be employed as NH_3 gas sensor devices, was successfully achieved. In the obtained semiconductor oxide layers, the less noble metal resulted in the form of isolated Cr(III) centers homogeneously dispersed in the WO_3 matrix, whereas platinum as Pt(0) metal nanoclusters anchored the WO_3 surface. Pt segregation may be related to the strong tendency of the WO_3 inverted opal array to remain undistorted, and to the easy reducibility of the noble metal ions in the presence of the poymethylmethacrylate templating agent.

The WO_3 semiconductor layers containing Pt nanoclusters revealed, upon exposure to NH_3, outstanding electrical properties even at relatively low operating temperature, and the sensitivity resulted as much higher than that of the undoped and Cr-doped layers. This behavior was attributed to the catalytic activation of N−H bond dissociation, which is suggested as the first step of NH_3 oxidation due to Pt nanoclusters anchored on the WO_3 surface. This electronic effect positively combines with the ability of the macroporous structure in promoting the effective gas diffusion within the entire sensing layer, leading to a sensitivity much higher than that of conventional sol−gel films with identical composition. Therefore, Pt-WO_3 inverse opal layers represent a very promising sensing material, easy to be obtained and to be used in chemical sensors with low energy consumption.

Furthermore, the simplicity of the one pot-procedure should, in principle, be applicable to prepare different crystalline macroporous materials, where the reproducibility of the morphology and the homogeneous embedding of dopants are required.

ASSOCIATED CONTENT

Supporting Information. The table reporting the electrical answers and recovery times for the Cr and Pt-doped WO_3 inverted opals, the elemental mapping of Cr in a Cr-doped WO_3 inverted opal thin film and SEM and TEM characterization of the

dx.doi.org/10.1021/ja109511a |J. Am. Chem. Soc. 2011, 133, 5296–5304

undoped WO_3 inverse opal films are reported. Details on the preparation procedure of conventional sol−gel films and their morphological characterization by TEM are also contained in this section. This material is available free of charge via the Internet at http://pubs.acs.org.

AUTHOR INFORMATION

Corresponding Author
massimiliano.darienzo1@unimib.it

ACKNOWLEDGMENT

The Milano group gratefully acknowledges the financial support of the Cariplo Foundation of Milano. The research was partially supported by Italian MIUR through the project FIRB RBPR05JH2P Rete ItalNanoNet. The authors also personally thank Luca Bollani for his support in the experimental part and Dr. Paolo Gentile for his assistance with SEM measurements.

REFERENCES

(1) Schroden, R. C. Stein, A. *3D Ordered Macroporous Material*; Wiley-VCH Verlag: Weinheim, Germany, 2004.
(2) Stein, A.; Li, F.; Denny, N. R. *Chem. Mater.* **2008**, *20*, 649–666.
(3) Qu, X.; Song, H.; Bai, X.; Pan, G.; Dong, B.; Zhao, H.; Wang, F.; Qin, R. *Inorg. Chem.* **2008**, *47*, 9654–9659.
(4) Qu, X.; Song, H.; Pan, G.; Bai, X.; Dong, B.; Zhao, H.; Dai, Q.; Zhang, H.; Qin, R.; Lu, S. J. *Phys. Chem. C* **2009**, *113*, 5906–5911.
(5) Waterhouse, G. I. N.; Metson, J. B.; Idriss, H.; Waterhouse, D. S. *Chem. Mater.* **2008**, *20*, 1183–1190.
(6) Arai, T.; Horiguchi, M.; Yanagida, M.; Gunjiab, T.; Sugiharaa, H.; Kazuhiro, S. *Chem. Commun.* **2008**, 5565–5567.
(7) Li, H.; Zhang, L.; Dai, H.; He, H. *Inorg. Chem.* **2009**, *48*, 4421–4434.
(8) Kim, J.; Lee, C. W.; Choi, W. *Environ. Sci. Technol.* **2010**, *44*, 6849–6854.
(9) Scott, R. W. J.; Yang, S. M.; Chabanis, G.; Coombs, N.; Williams, D. E.; Ozin, G. A. *Adv. Mater.* **2001**, *13*, 1468–1472.
(10) Scott, R. W. J.; Yang, S. M.; Coombs, N.; Williams, D. E.; Ozin, G. A. *Adv. Funct. Mater.* **2003**, *13*, 225–231.
(11) Acciarri, M.; Barberini, R.; Canevali, C.; Mari, C. M.; Mattoni, M.; Morazzoni, F.; Nodari, L.; Polizzi, S.; Ruffo, R.; Russo, U.; Sala, M.; Scotti, R. *Chem. Mater.* **2005**, *17*, 6167–6171.
(12) Sutti, A.; Baratto, C.; Calestani, G.; Dionigi, C.; Ferroni, M.; Faglia, G.; Sberveglieri, G. *Sens. Actuators B* **2008**, *130*, 567–573.
(13) Sasahara, K; Hyodo, T.; Shimizu, Y.; Egashira, M. *J. Eur. Ceram. Soc.* **2004**, *24*, 1961–1967.
(14) Lee, J. H. *Sens. Actuators B* **2009**, *140*, 319–336.
(15) Blanford, C. F.; Yan, H.; Schroden, R. C.; Al-Daous, M.; Stein, A. *Adv. Mater.* **2001**, *13*, 401–407.
(16) Sadakane, M.; Asanuma, T.; Kubo, J.; Ueda, W. *Chem. Mater.* **2005**, *17*, 3546–3551.
(17) Sadakane, M.; Takahashi, C.; Kato, N.; Asanuma, T.; Ogihara, H.; Ueda, W. *Chem. Lett.* **2006**, *35*, 480–481.
(18) Sadakane, M.; Horiuchi, T.; Kato, N.; Takahashi, C.; Ueda, W. *Chem. Mater.* **2007**, *19*, 5779–5785.
(19) Chen, X.; Li, Z.; Ye, J.; Zou, Z. *Chem. Mater.* **2010**, *22*, 3583–3585.
(20) Orilall, M. C.; Abrams, N. M.; Lee, J.; Di Salvo, F. J.; Wiesner, U. *J. Am. Chem. Soc.* **2008**, *130*, 8882–8883.
(21) Acciarri, M.; Canevali, C.; Mari, C. M.; Mattoni, M.; Ruffo, R.; Scotti, R.; Morazzoni, F.; Armelao, L.; Barreca, D.; Tondello, E.; Bontempi, E.; Depero, L. E. *Chem. Mater.* **2003**, *15*, 2646–2650.
(22) Scotti, R.; Canevali, C.; Mattoni, M.; Morazzoni, F.; Armelao, L.; Barreca, D. . In *Materials Syntheses*; Schubert, U., Husing, N., Laine, R., Eds.; Springer: New York, 2008; p 117.
(23) D'Arienzo, M.; Armelao, L.; Cacciamani, A.; Mari, C. M.; Polizzi, S.; Ruffo, R.; Scotti, R.; Testino, A.; Wahba, L.; Morazzoni, F. *Chem. Mater.* **2010**, *22*, 4083–4089.
(24) Jimenez, I.; Centeno, M. A.; Scotti, R.; Morazzoni, F.; Arbiol, J.; Cornet, A.; Morante, J. R. *J. Mater. Chem.* **2004**, *14*, 2412–2420.
(25) Morazzoni, F.; Scotti, R.; Origoni, L.; D'Arienzo, M.; Jimenez, I.; Cornet, A.; Morante, J. R. *Catal. Today* **2007**, *126*, 169–176.
(26) Epifani, M.; Andreu, T.; Arbiol, J.; Diaz, R.; Siciliano, P.; Morante, J. R. *Chem. Mater.* **2009**, *21*, 5215–5221.
(27) Breedon, M.; Spizzirri, P.; Taylor, M.; Plessis, J.; McCulloch, D.; Zhu, J.; Yu, L.; Hu, Z.; Rix, C.; Wlodarski, W.; Kalantar-zadeh, K. *Cryst. Growth Des.* **2010**, *10*, 430–439.
(28) Pinna, N.; Niederberger, M. *Angew. Chem., Int. Ed.* **2008**, *47*, 5292–5304 and references therein.
(29) Srivastava, V; Jain, K. *Sens. Actuators B* **2008**, *133*, 46–52.
(30) Senguttuvan, T. D.; Srivastava, V.; Tawal, J. S.; Mishra, M.; Srivastava, S.; Jain, K. *Sens. Actuators B* **2010**, *150*, 384–388.
(31) Rossinyol, E.; Prim, A.; Pellicer, E.; Arbiol, J.; Hernández-Ramírez, F.; Peiró, F.; Cornet, A.; Morante, J. R.; Solovyov, L. A.; Tian, B.; Bo, T.; Zhao, D. *Adv. Funct. Mater.* **2007**, *17*, 1801–1806.
(32) Zhao, Z. G.; Miyauchi, M. *J. Phys. Chem. C* **2009**, *113*, 6539–6546.
(33) Pokhrel, S.; Simion, C. E.; Teodorescu, V. S.; Barsan, N.; Weimar, U. *Adv. Funct. Mater.* **2009**, *19*, 1767–1774.
(34) Zamani, C.; Casals, O.; Andreu, T.; Morante, J. R.; Romano-Rodriguez, A. *Sens. Actuators B* **2009**, *140*, 557–562.
(35) Zhu, S.; Liu, X.; Chen, Z.; Liu, C.; Feng, C.; Gu, J.; Liu, Q.; Zhang, D. *J. Mater. Chem.* **2010**, *20*, 9126–9132.
(36) Sadakane, M.; Sasaki, K.; Kunioku, H.; Ohtani, B.; Abe, R.; Ueda, W. *J. Mater. Chem.* **2010**, *20*, 1811–1818.
(37) Sanchez, C.; Boissière, C.; Grosso, D.; Laberty, C.; Nicole, L. *Chem. Mater.* **2008**, *20*, 682–737.
(38) Schroden, R. C.; Al-Daous, M.; Blanford, C. F.; Stein, A. *Chem. Mater.* **2002**, *14*, 3305–3315.
(39) Briggs, D.; Seah, M. P. *Practical Surface Analysis*; J. Wiley: Chichester, U.K, 1990; Vol. 1.
(40) Moulder, J. F.; Stikle, W. F.; Sobol, P. E.; Bomben, K. D.; *Handbook of X-Ray Photoelectron Spectroscopy*; Perkin Elmer Corp.: Waltham, MA, 1992.
(41) Armelao, L.; Bertoncello, R.; Granozzi, G.; Depaoli, G.; Tondello, E.; Battaglin, G. *J. Mater. Chem.* **1994**, *4*, 407–411.
(42) Maekawa, T.; Tamaki, J.; Miura, N.; Yamazoe, N. *Chem. Lett.* **1992**, 639–642.
(43) Meixner, H.; Gerblinger, J.; Lampe, U.; Fleischer, M. *Sens. Actuators B* **1995**, *23*, 119–125.
(44) Lobet, E. G.; Molinas, P. M.; Calderer, J.; Vilanova, X.; Brezmes, J.; Sueiras, J. E.; Correig, X. *J. Electrochem. Soc.* **2000**, *147*, 776–779.
(45) Wang, G.; Ji, Y.; Huang, X.; Yang, X.; Gouma, P.; Dudley, M. *J. Phys. Chem. B* **2006**, *110*, 23777–23782.
(46) Mudiyanselage, K.; Trenary, M.; Meyer, R. J. *J. Phys. Chem. C* **2007**, *111*, 7127–7136.
(47) Jimenez, I.; Centeno, M. A.; Scotti, R.; Morazzoni, F.; Cornet, A.; Morante, J. R. *J. Electrochem. Soc.* **2003**, *150*, H72–H80.
(48) Epifani, M.; Andreu, T.; Magaña, C. R.; Diaz, R.; Arbiol, J.; Siciliano, P.; Morante, J. R. *Sens. Actuators B* **2010**, *148*, 200–206.
(49) Wang, X.; Miura, N.; Yamazoe, N. *Sens. Actuators B* **2000**, *65*, 163–165.
(50) Clifford, P. K.; Tuma, D. T. *Sens. Actuators* **1983**, *3*, 120.
(51) Schierbaum, K. D.; Weimar, U.; Gopel, W. *Sens. Actuators B* **1991**, *3*, 205–214.
(52) Park, C. O.; Akbar, S. A. *J. Mater. Sci.* **2003**, *38*, 4611–4637.
(53) Chabanis, G.; Parkin, I. P.; Williams, D. E. *Meas. Sci. Technol.* **2003**, *14*, 76–86.
(54) Williams, D. E.; Pratt, K. F. E. *Sens. Actuators B* **2000**, *70*, 214–221.